


Plasmons and magnetoplasmon resonances in nanoringsThomas Garm Pedersen ^{*}*Department of Materials and Production, Aalborg University, DK-9220 Aalborg Øst, Denmark*

(Received 19 October 2020; revised 2 February 2021; accepted 3 February 2021; published 12 February 2021)

Plasmonic sensors based on metallic nanorings benefit from resonances covering a wide spectral range and homogeneous cavity fields. Here, we explore the potential for nanorings in active plasmonics by examining the tunability of plasmon resonances due to external magnetic fields. Within the electrostatic approximation, we compute plasmon resonances and their shifts in magnetic fields for both solid and planar nanorings. In particular, solid nanorings of circular, elliptical, and disk-shaped cross sections are critically examined and compared to planar rings. Overall, we find that magnetoplasmon shifts in nanorings are greatly reduced compared to standard nanoparticles. However, flat geometries are found to be preferable and allow for relatively large shifts.

DOI: [10.1103/PhysRevB.103.085419](https://doi.org/10.1103/PhysRevB.103.085419)**I. INTRODUCTION**

Nanorings are useful in plasmonic sensors and related devices. Their plasmon resonances are highly sensitive to changes in surrounding analyte concentration and the local field inside the ring cavity is relatively homogeneous [1,2]. This is of practical importance for field enhancement in sensors designed to detect analytes placed at a distance from the nanoparticle surface, such as sensors relying on binding to antibodies [2]. Moreover, a wide range of resonance wavelengths are available by varying the ratio between inner and outer radii. Traditionally, solid nanorings have been fabricated from noble metals and support resonances across the visible or near-infrared range [1,2]. Recently, however, planar nanorings based on graphene have emerged [3], extending the range of available resonances far into the deep infrared.

While nanostructures with fixed resonances are normally considered, active plasmonics has recently been employed to increase device sensitivity [4–6]. By shifting plasmon resonances using external magnetic fields, it is possible to isolate the sensor response from background signals using lock-in or phase-sensitive detection. To this end, it is crucial that large magnetoplasmon shifts are obtained. For simple nanoparticles such as nanospheres and nanodisks, a perturbative analysis [7] shows that the maximal sensitivity to magnetic fields is found for ellipsoidal shapes including spheres. The simple explanation is that these shapes support plasmon modes, in which electrons always move in the plane perpendicular to the magnetic field, thereby maximizing the Lorentz force. Such modes are not found in, e.g., nanodisks, in which the internal electric field has significant out-of-plane components in the vicinity of corners [7].

In the present work, we extend the analysis of magnetoplasmon resonance shifts to nanoring geometries. We consider quite general geometries, in which a circular, elliptical, or disk-shaped cross section is revolved around a displaced axis of revolution, thereby producing a toroidal nanostructure as shown in Fig. 1(a). We restrict the analysis to the electrostatic

regime, in which the resonance eigenvalue problem is scale invariant [8–11]. Hence, resonances only depend on relative geometrical measures such as the ratio between inner and outer radii. The width of the cross section is $2a$ and the mean radius of the toroid is R . Hence, the axis of revolution, taken as the z axis, is displaced by R relative to the center of the cross section. We allow R to take values less than a , in which case a “spindle toroid” is formed; see Fig. 1(b). The border case $R = a$ produces a “horn toroid” and a true toroid with a punctured center is formed if $R > a$. We consider both solid nanorings as well as planar ones with a vanishing thickness. Such planar nanorings can be realized in graphene, in which sheet thickness is many orders of magnitude smaller than radii in the ring geometry [3].

By construction, the nanoring geometries are cylindrically symmetric. Moreover, the external magnetic field is assumed along the symmetry axis, as seen in Fig. 1(a). In this manner, cylindrical symmetry is preserved even in the presence of the field. This allows for a very efficient formulation of the localized surface plasmon resonance eigenvalue problem that essentially becomes one dimensional. Magnetoplasmons are sometimes grouped into edge, surface, and bulk plasmons depending on the characteristic trajectories of electrons. In the present approach, all types are handled on equal footing and we do not distinguish between them. In Refs. [7,10], techniques for treating the normal nanoparticle problem, i.e., taking $R = 0$, were presented. By extension of these techniques, we show how toroidal geometries can be handled similarly. Magnetoplasmon resonance shifts are found from a perturbative approach that takes the zero-magnetic-field eigenmode as input. Hence, the complicated problem of solving the eigenvalue problem in the presence of a magnetic field is circumvented in this manner. This enables us to compute resonance shifts (normalized by the cyclotron frequency) that are universal functions of geometrical ratios only.

II. SOLID NANORINGS

Solid nanoring geometries with cylindrical symmetry are constructed using the approach outlined in Fig. 1(b). Here, a circular, elliptical, or disk-shaped cross section defines the

^{*}tgp@mp.aau.dk

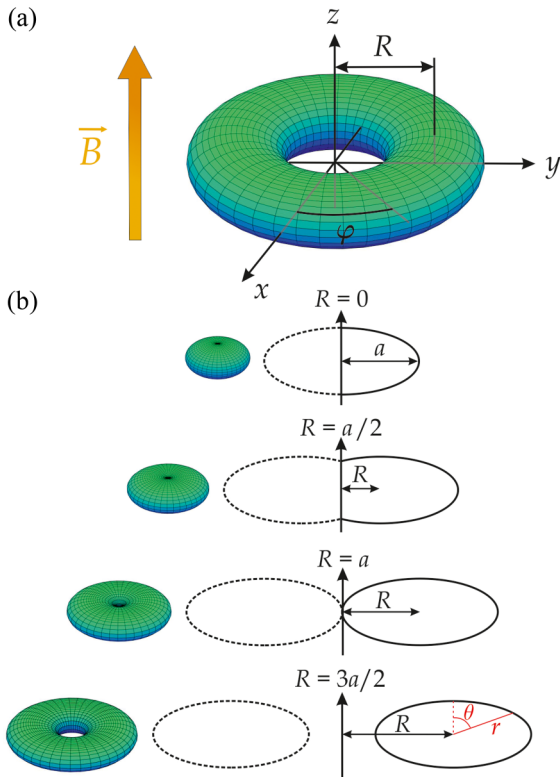


FIG. 1. Nanoring geometry. (a) Toroid in magnetic field aligned along the symmetry axis. (b) Toroidal geometries (left) generated from an elliptical cross section (right) by different radii of revolution R .

toroidal geometry when the radius of revolution R is specified. All structures are invariant under rotation by the azimuthal angle φ defined in Fig. 1(a). The cross sections themselves have horizontal widths of $2a$ and heights that may be both larger and smaller than $2a$. We parametrize a cross section by the polar angle θ and local radius $r = r(\theta)$ shown in the bottom panel of Fig. 1(b). The angle spans the range $\theta \in [\theta_-, \theta_+]$ that, in the case of a full toroid, is $\theta \in [-\pi/2, 3\pi/2]$ while a smaller range applies for a spindle toroid. In this manner, the plasmon eigenvalue problem is formulated using θ as the only variable, so that the problem is effectively one dimensional [10,11].

We note that electrostatic plasmon modes in nanotori assuming $R > a$ have previously been analyzed using toroidal coordinates [12,13]. These studies did not consider magnetic fields and were strictly limited to circular cross sections. Hence, this approach is not suited for the present work, in which a variety of cross sections are considered. Moreover, we find that the present approach is actually quite efficient computationally and converges rapidly as the angular grid is

refined. We use nonequidistant angular grids and take care to add many grid points near corners (based on local variation of the normal vector). As many as ~ 4000 grid points are applied for the most demanding geometries.

Throughout, we assume nanorings embedded in a homogeneous and isotropic medium with dielectric constant ε_1 . The nanoring itself is characterized by an isotropic but frequency-dependent dielectric constant $\varepsilon(\omega)$ in the absence of a magnetic field. However, in an external field $\vec{B} = B\hat{z}$ or, equivalently, internal magnetization aligned along z , the nanoring response is of the gyrotropic form [14],

$$\vec{\varepsilon} = \begin{pmatrix} \varepsilon_{xx} & \varepsilon_{xy} & 0 \\ -\varepsilon_{xy} & \varepsilon_{xx} & 0 \\ 0 & 0 & \varepsilon_{zz} \end{pmatrix}. \quad (1)$$

In a lossless Drude metal with plasma frequency ω_p and cyclotron frequency $\omega_c = eB/m_e$, we have [14–16] $\varepsilon_{zz} = \varepsilon_\infty - \omega_p^2/\omega^2$, $\varepsilon_{xx} = \varepsilon_\infty - \omega_p^2/(\omega^2 - \omega_c^2)$, and $\varepsilon_{xy} = i\omega_c\omega_p^2/[\omega(\omega^2 - \omega_c^2)]$. Hence, corrections due to the magnetic perturbation are of second or higher order for the diagonal tensor elements. The off-diagonal response ε_{xy} , however, is proportional to B in a first-order approximation. This, therefore, is the dominant effect in weak fields and leads to Faraday rotation and related phenomena with a linear B -field dependence. Hence, as an approximation valid in weak fields $\varepsilon_{xx} \approx \varepsilon_{zz} \equiv \varepsilon = \varepsilon_\infty - \omega_p^2/\omega^2$ and $\varepsilon_{xy}(\omega) \approx i\omega_c\omega_p^2/\omega^3$. Below, we apply this simplified form but higher order corrections are discussed in Sec. IV.

Plasmon modes are classified as either vertical (z direction) or horizontal (x, y plane), as dictated by the polarization of the incident excitation. We apply the surface charge approach to formulate the eigenvalue problem [7–11]. This is a highly computationally efficient framework, in which a geometry-dependent integral equation provides plasmon resonances. In the electrostatic regime, a given geometry leads to characteristic eigenvalues that subsequently translate into actual frequencies once a dielectric constant is specified for the material; see, e.g., Refs. [7–11] for examples. A position on the nanoring surface is specified by the angles (θ, φ) . For a vertical eigenmode, symmetry demonstrates that surface charge σ is independent of azimuthal angle φ , i.e., $\sigma = \sigma(\theta)$. In contrast, horizontal eigenmodes vary as $\sigma_\pm(\theta) \exp(\pm i\varphi)$. To linear order in the magnetic field, the vertical plasmon modes are unaffected and their eigenvalue condition reads [7]

$$\sigma(\theta) = \frac{\varepsilon - \varepsilon_1}{\varepsilon + \varepsilon_1} \int_{\theta_-}^{\theta_+} G_n^{(v)}(\theta, \theta') \sigma(\theta') S(\theta') d\theta'. \quad (2)$$

The horizontal modes, in contrast, are modified by the magnetic perturbation and their eigenvalue problem is of the form

$$\sigma_\pm(\theta) = \frac{\varepsilon - \varepsilon_1}{\varepsilon + \varepsilon_1} \int_{\theta_-}^{\theta_+} \left\{ G_n^{(h)}(\theta, \theta') \pm \frac{i\varepsilon_{xy}}{\varepsilon - \varepsilon_1} F_\varphi^{(h)}(\theta, \theta') \right\} \sigma_\pm(\theta') S(\theta') d\theta'. \quad (3)$$

In these expressions, the integral kernels are given by

$$G_n^{(v)}(\theta, \theta') = [n_z(r \cos \theta - r' \cos \theta') + n_x(R + r \sin \theta)] F_{0,1}(x, y) - n_x(R + r' \sin \theta') F_{1,1}(x, y), \quad (4)$$

and

$$\begin{aligned} G_n^{(h)}(\theta, \theta') &= [n_z(r \cos \theta - r' \cos \theta') + n_x(R + r \sin \theta)]F_{1,1}(x, y) - n_x(R + r' \sin \theta')F_{2,1}(x, y), \\ F_\varphi^{(h)}(\theta, \theta') &= n_x(R + r' \sin \theta')[F_{0,1}(x, y) - F_{2,1}(x, y)], \end{aligned} \quad (5)$$

for the vertical and horizontal cases, respectively, with n_i the Cartesian components of the normal vector at angle θ . The $F_{m,n}(x, y)$ functions are defined in Ref. [10] and their arguments are

$$x = r^2 + r'^2 - 2rr' \cos \theta \cos \theta' + 2R^2 + 2R(r \sin \theta + r' \sin \theta'), \quad y = -2(R + r \sin \theta)(R + r' \sin \theta'). \quad (6)$$

The expressions in Eqs. (4)–(6) are generalizations of the corresponding results derived for cylindrically symmetric nanoparticles to allow for a finite radius of revolution R and agree with previous expressions [10] in the limiting case $R = 0$. Similarly, a surface area element in the toroidal geometry is $dS = S(\theta)d\theta d\varphi$ with area function $S(\theta)$ generalized to the $R \neq 0$ case, i.e., $S(\theta) = r(\theta)(R + r(\theta) \sin \theta)/(n_x \sin \theta + n_z \cos \theta)$.

The perturbative solution for the horizontal case in Eq. (3) starts from solving the unperturbed problem

$$\sigma_0(\theta) = \lambda_0 \int_{\theta_-}^{\theta_+} G_n^{(h)}(\theta, \theta') \sigma_0(\theta') S(\theta') d\theta' \quad (7)$$

to obtain the zeroth-order eigenfunction $\sigma_0(\theta)$ and eigenvalue $\lambda_0 = [\varepsilon(\omega_0) - \varepsilon_1]/[\varepsilon(\omega_0) + \varepsilon_1]$. Here, ω_0 is the unperturbed plasmon resonance that can be found provided a specific model for $\varepsilon(\omega)$ is assumed. Collecting first-order terms in Eq. (3), the perturbed eigenvalue becomes

$$\lambda \approx \lambda_0 \pm \frac{i\varepsilon_{xy}(\omega_0)\lambda_0(\lambda_0 - 1)}{2\varepsilon_1} \int_{\theta_-}^{\theta_+} \int_{\theta_-}^{\theta_+} \sigma_0^\dagger(\theta) F_\varphi^{(h)}(\theta, \theta') \sigma_0(\theta') S(\theta') d\theta' d\theta, \quad (8)$$

where $\sigma_0^\dagger(\theta)$ is the adjoint eigenfunction. This implies the simple shifted resonances $\omega_\pm = \omega_0 \pm \frac{1}{2} \Delta\omega$ with

$$\Delta\omega \approx \omega_c \frac{\lambda_0}{\lambda_0 - 1} \int_{\theta_-}^{\theta_+} \int_{\theta_-}^{\theta_+} \sigma_0^\dagger(\theta) F_\varphi^{(h)}(\theta, \theta') \sigma_0(\theta') S(\theta') d\theta' d\theta. \quad (9)$$

If a dispersive interband response $\varepsilon_\infty(\omega) \approx \varepsilon_\infty(\omega_0) + \varepsilon'_\infty(\omega_0)(\omega - \omega_0)$ is allowed for, the shift is multiplied by an additional factor of $[1 + \varepsilon'_\infty(\omega_0)\omega_0^3/(2\omega_p^2)]^{-1}$. Since, generally, the resonance ω_0 is significantly smaller than the bare plasma frequency ω_p in metallic nanoparticles, the extra factor is close to unity. It is conceivable, however, that the shift could be enhanced by exploiting spectral regions of anomalous interband dispersion, i.e., $\varepsilon'_\infty(\omega_0) < 0$. The perturbed resonances ω_\pm are symmetrically displaced by $\pm \frac{1}{2} \Delta\omega$ relative to ω_0 . The splitting $\Delta\omega$ itself is found to be positive for the lowest plasmon in all structures. For higher plasmons with a more complicated mode structure, however, negative values occur.

We first analyze the bare plasmon modes in the absence of magnetic perturbations. As representative geometries, we select toroids formed from cross sections that are circular, prolate, and oblate elliptical, and disk-shaped with corners rounded by radii of $h/4$. In Fig. 2, vertical and horizontal modes are depicted as blue and red curves, respectively, for Ag nanorings ($\hbar\omega_p = 9.3$ eV and $\varepsilon_\infty = 5$) in air ($\varepsilon_1 = 1$). The vertical and horizontal nanoparticle modes at $R = 0$ behave as expected. Thus, modes are degenerate for spheres, while modes polarized along nanoparticle long axes are redshifted compared to short-axes modes for ellipsoids and disks. As R is increased, horizontal modes redshift further, while vertical modes blueshift or remain approximately constant. Accordingly, the modes cross for prolate ellipsoids near the formation of a horn toroid at $R = a$. The “flat” nanorings, i.e., oblate elliptical or disk-shaped, provide the largest red-

shifts. Hence, horizontal plasmon modes in such geometries are suitable for obtaining resonances in the infrared. Similar findings are known from flattened solid nanoparticles such as oblate ellipsoids [11]. The surface charge distributions in

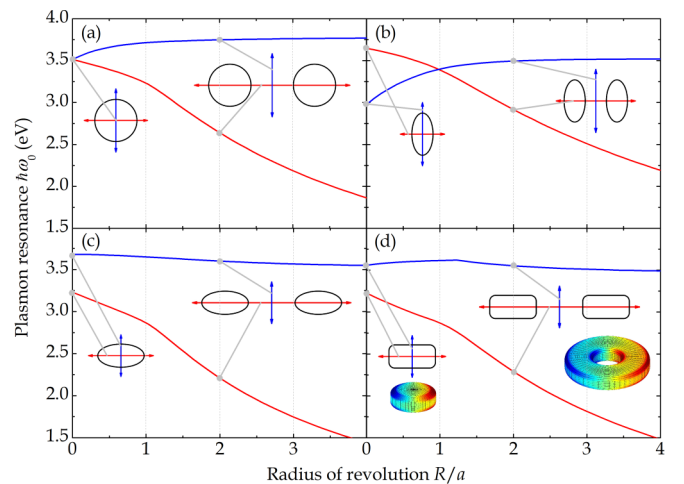


FIG. 2. Toroid resonances for vertical (blue) and horizontal (red) modes of Ag nanorings in air. The applied cross sections shown at $R = 0$ have different height/width ($h/2a$) ratios. The panels show (a) spherical $h/2a = 1$, (b) prolate elliptical $h/2a = 2$, (c) oblate elliptical $h/2a = 1/2$, and (d) disk-shaped $h/2a = 1/2$ cross sections, respectively. Surface charge distributions for $R/a = 0$ and 2 are included in (d).

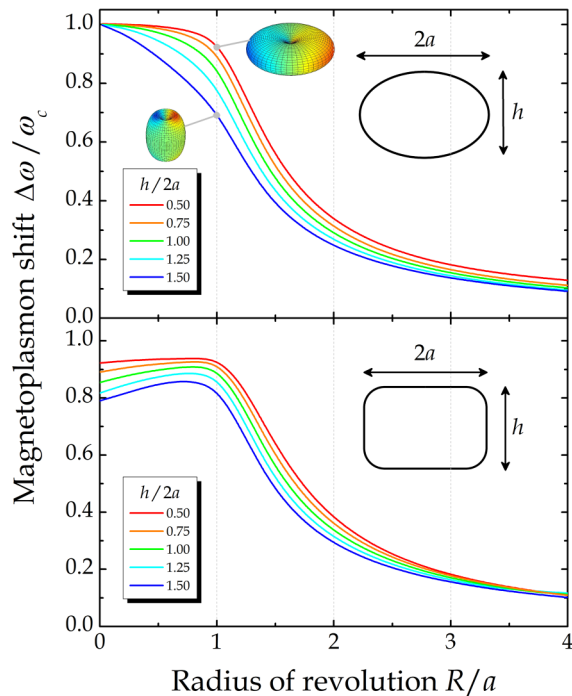


FIG. 3. Magnetoplasmon shifts of nanorings based on elliptical (top panel) and disk-shaped (bottom panel) cross sections. For disks, rounding radii at the corners are $h/4$. Surface charge distributions are shown for flattened and barrel-shaped horn toroids ($R = a$) with elliptical cross section.

Fig. 2(d) demonstrate that a much larger dipole is induced in the nanoring compared to a nanoparticle with the same cross section, due to the larger lateral extent. Also, in nanorings opposite segments of the ring are oppositely charged and, thereby, concentrate the electric field in the ring cavity. This, essentially, is the reason behind the homogeneous cavity field mentioned above.

Next, we turn to the magnetoplasmon resonances. We aim to determine how the cross-sectional height/width ratio as well as the radius of revolution affect the magnetoplasmon shift $\Delta\omega$. Clearly, a large value of $\Delta\omega$ is desirable for active plasmonics. As will be made apparent, however, redshifting resonances by forming nanorings rather than nanoparticles leads to a substantial reduction of the magnetoplasmon shift. Our results are based on Eq. (9), which is universally valid for Drude metals and only requires geometrical input. Moreover, within scale-invariant electrostatics, only ratios such as $h/2a$ and R/a matter.

Results for elliptical and disk-shaped cross sections are illustrated in Fig. 3. Ellipses are special, in that $\Delta\omega/\omega_c = 1$ at $R = 0$ irrespective of ellipticity. Again, this is a consequence of the strictly horizontal internal field allowed by these geometries. In contrast, shifts decrease for disks as their heights increase, in agreement with Ref. [7]. A clear trend supported by both geometries is that flatter structures are better as they lead to larger shifts. This finding is explained by comparing the surface charge distributions shown for flat and barrel-shaped nanorings. Surface charges accumulate in regions having a large curvature, which means that dipoles form only in the top and bottom portions of the $h/2a = 1.5$

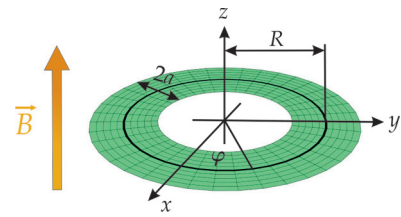


FIG. 4. Planar nanoring with mean radius R and width $2a$ in perpendicular magnetic field.

barrel toroid. In contrast, the flat nanoring with $h/2a = 0.5$ supports a dipole across the central part. As a consequence, the internal electric field has a large horizontal component, which translates into a large magnetoplasmon shift due to the Lorentz force that is maximal for perpendicular electric and magnetic fields. Hence, such flat geometries appear to support useful shifts. However, the shift decreases dramatically as the toroidal geometry expands. Thus, around $R \sim 4a$, shifts are reduced to roughly 10% of their nanoparticle values. This must be contrasted with the resonance frequency itself, which only decreases by about 50%, cf. Fig. 2. Hence, the relative shift is still reduced to 20–30% of the nanoparticle result. As a consequence, active plasmonics based on magnetoplasmon shifts in nanorings appears less promising. The homogeneous field provided by the cavity may still render ring geometries attractive for sensing purposes, however, and it is important to identify designs allowing for relatively large magnetoplasmon shifts in active nanoring plasmonic sensors.

III. PLANAR NANORINGS

Nanostructured graphene has extended the range of available geometries to a different regime, in which height is orders of magnitude smaller than other characteristic measures such as a and R in nanorings. An appropriate description of these planar geometries starts from the premise that the material has zero thickness [17–21]. In this manner, the plasmonic response is formulated in terms of the sheet instead of bulk response. Conventionally, the graphene response is expressed via the conductivity rather than susceptibility. For the Drude metal discussed above, the bulk conductivities are $\sigma(\omega) = i\varepsilon_0\omega(\omega_p^2/\omega^2 + 1 - \varepsilon_\infty)$ and $\sigma_{xy}(\omega) = \varepsilon_0\omega_c\omega_p^2/\omega^2$. The corresponding sheet quantities are simply obtained by multiplying with the sheet thickness h . In narrow graphene rings and small disks, pronounced quantum confinement effects are observed in the magnetic properties [22]. In the present work, however, we restrict the analysis to structures big enough to allow for use of the bulk response.

The geometries analyzed are illustrated in Fig. 4. These can be thought of as infinitely flattened versions of the solid nanorings considered in the previous section, rendering the geometry two dimensional. Since cylindrical symmetry is still preserved, potential modes are of the form $\phi_{\pm}^{(l)}(r)e^{\pm il\varphi}$ with radial coordinate $r = (x^2 + y^2)^{1/2}$ and $l > 0$ integer. The planar version of the plasmon eigenmode problem for angular momentum l reads [20]

$$\begin{aligned} \lambda \phi_{\pm}^{(l)}(r) = & -R_+ \int_{R_-}^{R_+} K_l(r, r') \left\{ \frac{d}{dr'} r' \frac{d}{dr'} - \frac{l^2}{r'^2} \right\} \phi_{\pm}^{(l)}(r') dr' \\ & \pm \frac{i l \sigma_{xy}(\omega)}{\sigma(\omega)} R_+ \{ K_l(r, R_+) \phi_{\pm}^{(l)}(R_+) - K_l(r, R_-) \phi_{\pm}^{(l)}(R_-) \} \end{aligned} \quad (10)$$

with eigenvalue $\lambda = 2i\omega\varepsilon_1\varepsilon_0R_+/\sigma(\omega)h$, where the outer and inner radii are $R_+ = R + a$ and $R_- = \max(R - a, 0)$, respectively, reflecting the fact that the inner radius is zero if $R < a$. Note that both sides of Eq. (10) have been multiplied by factors of R_+ for convenience and that, on the left-hand side, this factor is absorbed into the definition of the eigenvalue to make it dimensionless. For a disk, i.e., if $R_- = 0$, the eigenvalue is independent of R_+ , as is readily shown by scaling $r \rightarrow r/R_+$. In turn, since $\lambda = 2i\omega\varepsilon_1\varepsilon_0R_+/\sigma(\omega)h$, the resonance frequency ω must depend on R_+ to keep λ fixed. Hence, for a free-electron Drude metal with $\varepsilon_{\infty} = 1$ such as graphene this means that $\omega \propto R_+^{-1/2}$. The K_l integral kernel is

$$K_l(r, r') = \frac{1}{2\pi} \int_0^{2\pi} \frac{\cos l\varphi}{\sqrt{r^2 + r'^2 - 2rr' \cos \varphi}} d\varphi. \quad (11)$$

For the important dipole mode with $l = 1$, $K_1(r, r') = F_{1,0}(r^2 + r'^2, -2rr')$, i.e., one of the F functions introduced in the previous section.

First, we consider the unperturbed problem by setting $\sigma_{xy} = 0$. In this case,

$$\lambda_0 \phi_0^{(l)}(r) = -R_+ \int_{R_-}^{R_+} K_l(r, r') \left\{ \frac{d}{dr'} r' \frac{d}{dr'} - \frac{l^2}{r'^2} \right\} \phi_0^{(l)}(r') dr'. \quad (12)$$

Here, λ_0 and $\phi_0^{(l)}$ are the unperturbed eigenvalue and eigenfunction, respectively. We introduce the adjoint eigenfunctions $\phi_0^{(l)\dagger}$ in the planar case and normalize according to $\int_{R_-}^{R_+} \phi_0^{(l)\dagger}(r) \phi_0^{(l)}(r) dr = 1$. In analogy with the solid nanoring case, a perturbation analysis of the full problem then yields

$$\begin{aligned} \lambda \approx \lambda_0 \mp \lambda_0 \frac{i\sigma_{xy}(\omega_0)}{\sigma(\omega_0)} R_+ \int_{R_-}^{R_+} \phi_0^{(l)\dagger}(r) \{ & K_l(r, R_+) \phi_0^{(l)}(R_+) \\ & - K_l(r, R_-) \phi_0^{(l)}(R_-) \} dr. \end{aligned} \quad (13)$$

By analyzing the relation between eigenvalue and resonance frequency, it is readily established that for a general Drude metal with arbitrary ω_p and ε_{∞} we again find resonances at $\omega = \omega_0 \pm \frac{1}{2} \Delta\omega$ with a normalized shift (to first order)

$$\begin{aligned} \frac{\Delta\omega}{\omega_c} \approx \frac{R_+}{\lambda_0} \int_{R_-}^{R_+} \phi_0^{(l)\dagger}(r) \{ & K_l(r, R_+) \phi_0^{(l)}(R_+) \\ & - K_l(r, R_-) \phi_0^{(l)}(R_-) \} dr. \end{aligned} \quad (14)$$

Our computational approach is based on solving Eq. (12) and subsequently using Eq. (14) to evaluate the plasmon shift. To this end, an equidistant radial grid containing 750 grid points is applied. We use midpoint sampling [23] and discretize both K_l and the radial Laplacian. If the radial grid spacing is Δr , the discretized Coulomb kernel is approxi-

mated by

$$\begin{aligned} K_{ij} & \equiv \int_{r_j - \Delta r/2}^{r_j + \Delta r/2} K_1(r_i, r') dr' \\ & \approx \begin{cases} K_1(r_i, r_j) \Delta r & i \neq j \\ -\frac{\Delta r}{\pi r_i} \left\{ 1 + \ln \left(\frac{\Delta r}{16r_i} \right) \right\} & i = j. \end{cases} \end{aligned} \quad (15)$$

We note that the matrix problem in Eq. (12) is not Hermitian and so $\phi_0^{(l)\dagger} \neq \phi_0^{(l)}$.

In Fig. 5, we show the unperturbed eigenvalue λ_0 and normalized magnetoplasmon shift versus geometric ratios in planar nanorings for the dipole mode $l = 1$. The eigenvalues agree with previous results based on an entirely different numerical approach, i.e., expansion in a finite basis [18]. For an unpunctured nanodisk $R_- = 0$, the lowest eigenvalue is $\lambda_0 = 1.098$ and the shift is $\Delta\omega/\omega_c = 0.921$. This should be contrasted with the value $\Delta\omega/\omega_c = 1$ found if a disk is approximated by a thin ellipsoid [21]. Clearly, this approximation is not quantitatively correct. Both eigenvalue and shift decrease monotonically as the ring becomes narrower and

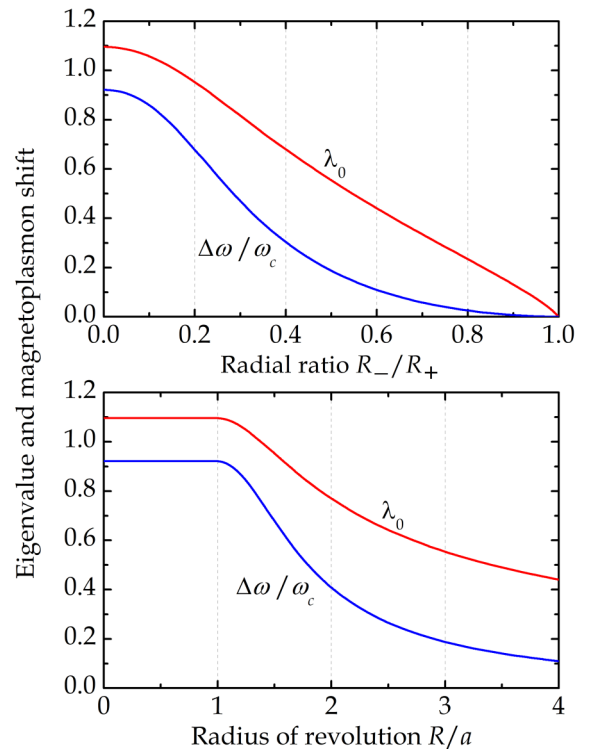


FIG. 5. Magnetoplasmon shift in planar nanorings. The same data are shown versus ratio between inner and outer radii (top panel) and normalized radius of revolution (bottom panel). Note that for $R \leq a$ the disk remains unpunctured and, hence, eigenvalue and shift are independent of R in this range.

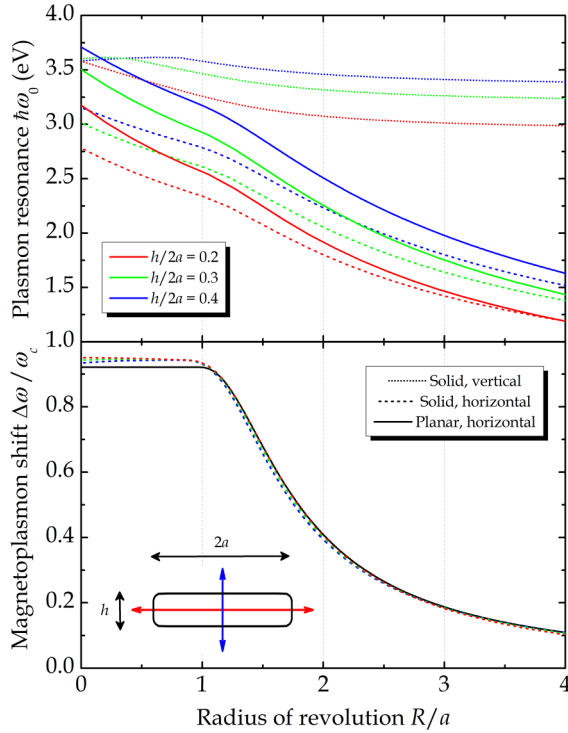


FIG. 6. Comparison of solid nanorings based on thin nanodisks (dashed and dotted lines) and their planar approximations (solid lines) for different heights as indicated by color. Plasmon resonances and magnetoplasmon shifts are in upper and lower panels, respectively. Rounding radii of solid structures are $h/4$.

vanish in the extreme limit $R_- \approx R_+$. For Drude metals, the resonance follows $\omega_0 \propto \lambda_0^{1/2}$ (see below) and, so, the results show that both plasmon resonance and shift decrease as the hole expands. The decrease of the plasmon shift, however, is more rapid and as a consequence the relative shift is reduced.

Finally, we study the convergence of both unperturbed and perturbed plasmons in solid nanorings towards the planar approximation as h decreases. Hence, for unperturbed planar nanorings, we solve Eq. (12) and retrieve the resonance from $\omega_0 = \omega_p / (2\varepsilon_1 R_+ / \lambda_0 h + \varepsilon_\infty - 1)^{1/2}$. In the strict 2D limit $h \rightarrow 0$, one has $\omega_0 \approx \omega_p^{(2D)} \lambda_0^{1/2} / (2\varepsilon_1 R_+)^{1/2}$ with 2D plasma frequency $\omega_p^{(2D)} = \omega_p \sqrt{h}$. In Fig. 6, we compare the planar approximation to results using Eq. (7) for solid but increasingly thin nanorings. The planar theory only captures the horizontal mode, so no comparison is made for the vertical one. The solid structures are rounded by $h/4$ radius quarter circles to reduce the effect of corners, as shown in the inset in Fig. 6.

The comparison in Fig. 6 demonstrates that the planar model is a reasonable approximation for flat solid nanorings with $h/2a \leq 0.2$. In particular, at $R = 0$, the normalized magnetoplasmon shift in the lower panel of Fig. 6 is found to be $\Delta\omega/\omega_c \approx 0.95$ for solid nanorings with $h/2a = 0.2$, which deviates by about 3% from the planar approximation $\Delta\omega/\omega_c = 0.921$. Moreover, solid nanorings with $R \leq a$, i.e., nanodisks, have roughly constant shifts irrespective of R . This, again, is in agreement with the expectations from the planar model, in which the shift is the same for all unpunctured disks,

i.e., for all $R \leq a$. For true toroids with a punctured center, the magnetoplasmon shifts of solid and planar structures are in excellent agreement. Regarding the plasmon resonances themselves in the upper panel of Fig. 6, it is seen that deviations of order 10% are found for the horizontal modes. The planar approximation does not support vertical modes, which is clearly a deficiency of the model.

IV. EFFECTS OF INTERBAND DISPERSION AND MAGNETIC NONLINEARITY

The theory analyzed so far has been based on the simple Drude form for the dielectric tensor assuming constant interband response and ignoring second and higher order magnetic effects. We now study the more general case in order to validate the applied simplifications. Hence, we consider the generalized dielectric response

$$\begin{aligned} \varepsilon_{xx}(\omega) &= \varepsilon_\infty(\omega) - \frac{\omega_p^2}{\omega^2 - \omega_c^2}, & \varepsilon_{zz}(\omega) &= \varepsilon_\infty(\omega) - \frac{\omega_p^2}{\omega^2}, \\ \varepsilon_{xy}(\omega) &= \frac{i\omega_c \omega_p^2}{\omega(\omega^2 - \omega_c^2)}. \end{aligned} \quad (16)$$

Apart from nonlinearities arising from ω_c^2 , we include a realistic interband response $\varepsilon_\infty(\omega)$ found by subtracting the intraband part from the experimental response $\varepsilon_{\text{exp}}(\omega)$ from Johnson and Christy [24], i.e., $\varepsilon_\infty(\omega) = \text{Re}\{\varepsilon_{\text{exp}}(\omega) + \omega_p^2/\omega^2\}$, similarly to the approach in Ref. [25]. Since $\varepsilon_{xx} \neq \varepsilon_{zz}$, the eigenvalue problem assumes a significantly more complicated form [7],

$$\begin{aligned} \sigma_\pm(\theta) &= \frac{1}{\varepsilon_{xx}n_x^2 + \varepsilon_{zz}n_z^2 + \varepsilon_1} \int_{\theta_-}^{\theta_+} \{(\varepsilon_{xx} - \varepsilon_1)G_n^{(h)}(\theta, \theta') \\ &\quad + (\varepsilon_{zz} - \varepsilon_{xx})G_z^{(h)}(\theta, \theta') \pm i\varepsilon_{xy}F_\varphi^{(h)}(\theta, \theta')\} \\ &\quad \times \sigma_\pm(\theta')S(\theta')d\theta', \end{aligned} \quad (17)$$

with the z component of the Green's function $G_z^{(h)}(\theta, \theta') = n_z(r \cos \theta - r' \cos \theta')F_{1,1}(x, y)$. We solve this equation by sweeping over frequency and locating unit eigenvalues of the right-hand side.

As a practical application of relevance, we now look at Ag nanorings having a circular cross section such as those in Fig. 2(a). Here, however, we include full dispersion of the interband response. In Fig. 7, numerical resonances obtained from Eq. (17) are compared to the linearized theory in Eq. (9), both with and without accounting for interband dispersion. To obtain reliable derivatives, we fit experimental interband data to a third degree polynomial as shown in the inset in Fig. 7. It is seen that interband dispersion is relatively more important at high frequencies, i.e., for less flattened geometries. The two panels in the figure correspond to $R/a = 1$ and 2 representing horn and true tori, respectively. Nonlinear magnetic effects are observed above $\hbar\omega_c \sim 0.1$ eV, which requires a magnetic field of $B \sim 860$ T applying the free-electron mass $m_e \approx m_0$ for conversion. At this field, the magnetoplasmon shift is roughly 1% of the unperturbed resonance for $R/a = 1$. Thus, nonlinear effects are difficult to observe experimentally. Below this field, the linearized theory is in excellent agreement with the full simulation, especially if interband dispersion is included.

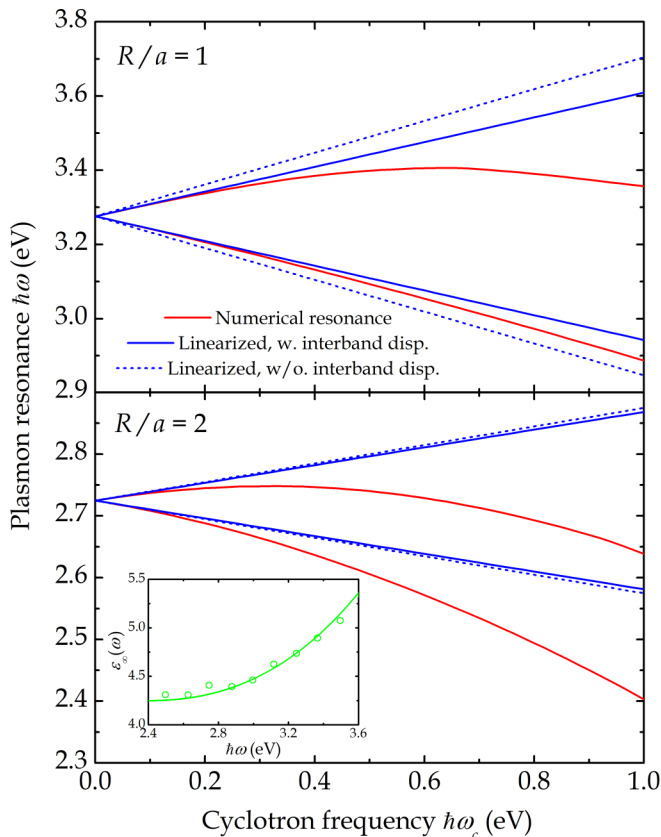


FIG. 7. Numerical resonances for Ag nanotori based on measured interband dispersion and including magnetic nonlinearities for two different radii of revolution (red curves). For comparison, linearized approximations with (solid lines) and without (dashed lines) interband dispersion are shown in blue. Inset: Experimental interband response (circles [24]) and polynomial fit.

This is particularly clear at higher energies, at which neglecting interband dispersion leads to significant overestimation of the magnetoplasmon shift, cf. dashed curves in Fig. 7.

In addition, it is noted that nonlinearity tends to reduce the plasmon resonances. This is in contrast to solid nanospheres with unperturbed resonance ω_0 , for which an upward correction given by $\omega_{\pm} = (\omega_0^2 + \omega_c^2/4)^{1/2} \pm \omega_c/2$ is found [26], as we have verified using the present approach. The downward correction is indicative of nanorings and has previously been observed experimentally in GaAs nanorings [18]. Such nonlinearities are accessible in certain semiconductors due to their small effective mass ($m_e \approx 0.06m_0$ in GaAs) leading to large cyclotron frequencies at relatively small magnetic fields. In metallic systems, however, observing such effects is challenging. We therefore conclude that the linearized theory presented above is likely to remain highly accurate when applied to real metallic nanostructures, especially if interband dispersion is accounted for.

V. SUMMARY

Summarizing, we have studied the plasmon properties of nanorings perturbed by magnetic fields. Efficient perturbative computational approaches have been developed for both solid and planar nanorings with cylindrical symmetry. Generally, the sensitivity to magnetic fields is found to decrease as the nanoring cross section is made narrower. Thus, the magnetoplasmon shift is reduced to less than 10% of the value for ellipsoidal nanoparticles if the ratio between inner and outer radii exceeds 60%. Overall, flat structures have larger shifts and planar (two-dimensional) rings outperform solid ones for narrow rings. Finally, the perturbation approach has been validated by comparison to full numerical simulation for Ag nanorings based on experimental dielectric response and including magnetic nonlinearities.

ACKNOWLEDGMENTS

The author acknowledges stimulating discussions with F. Pineider and the QUSCOPE center funded by the Villum foundation for financial support.

- [1] J. Aizpurua, P. Hanarp, D. S. Sutherland, M. Käll, G. W. Bryant, and F. J. García de Abajo, *Phys. Rev. Lett.* **90**, 057401 (2003).
- [2] E. M. Larsson, J. Alegret, M. Käll, and D. S. Sutherland, *Nano Lett.* **7**, 1256 (2007).
- [3] Z. Fang, S. Thongrattanasiri, A. Schlather, Z. Liu, L. Ma, Y. Wang, P. M. Ajayan, P. Nordlander, N. J. Halas, and F. J. García de Abajo, *ACS Nano* **7**, 2388 (2013).
- [4] V. Bonanni, S. Bonetti, T. Pakizeh, Z. Pirzadeh, J. Chen, J. Nogués, P. Vavassori, R. Hillenbrand, J. Åkerman, and A. Dmitriev, *Nano Lett.* **11**, 5333 (2011).
- [5] F. Pineider, G. Campo, V. Bonanni, C. de Julián Fernández, G. Mattei, A. Caneschi, D. Gatteschi, and C. Sangregorio, *Nano Lett.* **13**, 4785 (2013).
- [6] N. Maccaferri, K. E. Gregorczyk, T. V. De Oliveira, M. Kataja, S. Van Dijken, Z. Pirzadeh, A. Dmitriev, J. Åkerman, M. Knez, and P. Vavassori, *Nat. Commun.* **6**, 6150 (2015).
- [7] T. G. Pedersen, *Phys. Rev. B* **102**, 075410 (2020).
- [8] I. D. Mayergoyz, D. R. Fredkin, and Z. Zhang, *Phys. Rev. B* **72**, 155412 (2005).
- [9] I. D. Mayergoyz and Z. Zhang, *IEEE Trans. Magn.* **42**, 759 (2006).
- [10] J. Jung, T. G. Pedersen, T. Søndergaard, K. Pedersen, A. N. Larsen, and B. Bech Nielsen, *Phys. Rev. B* **81**, 125413 (2010).
- [11] J. Jung, T. G. Pedersen, T. Søndergaard, K. Pedersen, A. N. Larsen, and B. Bech Nielsen, *Phys. Status Solidi RRL* **4**, 292 (2010).
- [12] C. M. Dutta, T. A. Ali, D. W. Brandl, T.-H. Park, and P. Nordlander, *J. Chem. Phys.* **129**, 084706 (2008).
- [13] K. V. Garapati, M. Salhi, S. Kouchekian, G. Siopsis, and A. Passian, *Phys. Rev. B* **95**, 165422 (2017).
- [14] G. W. Ford and S. A. Werner, *Phys. Rev. B* **18**, 6752 (1978).
- [15] G. Armelles, A. Cebollada, A. García-Martín, and M. U. González, *Adv. Opt. Mater.* **1**, 10 (2013).
- [16] Z. Yu, G. Veronis, Z. Wang, and S. Fan, *Phys. Rev. Lett.* **100**, 023902 (2008).

- [17] C. Dahl, J. P. Kotthaus, H. Nickel, and W. Schlapp, *Phys. Rev. B* **48**, 15480 (1993).
- [18] V. A. Kovalskii, S. I. Gubarev, I. V. Kukushkin, S. A. Mikhailov, J. H. Smet, K. von Klitzing, and W. Wegscheider, *Phys. Rev. B* **73**, 195302 (2006).
- [19] F. A. Reboredo and C. R. Proetto, *Phys. Rev. B* **53**, 12617 (1996).
- [20] W. Wang, *J. Phys.: Condens. Matter* **24**, 402202 (2012).
- [21] W. Wang, S. P. Apell, and J. M. Kinaret, *Phys. Rev. B* **86**, 125450 (2012).
- [22] M. R. Thomsen and T. G. Pedersen, *Phys. Rev. B* **95**, 235427 (2017).
- [23] T. Christensen, W. Yan, A.-P. Jauho, M. Wubs, and N. A. Mortensen, *Phys. Rev. B* **92**, 121407(R) (2015).
- [24] P. B. Johnson and R. W. Christy, *Phys. Rev. B* **6**, 4370 (1972).
- [25] E. J. H. Skjølstrup, T. Søndergaard, and T. G. Pedersen, *Phys. Rev. B* **97**, 115429 (2018).
- [26] R. P. Devaty, *Phys. Rev. B* **38**, 7972 (1988).